

Flopping-mode spin qubit in a Si-MOS quantum dot

Rui-Zi Hu,^{1, 2, a)} Rong-Long Ma,^{1, 2, a)} Ming Ni,^{1, 2} Yuan Zhou,^{1, 2} Ning Chu,^{1, 2} Wei-Zhu Liao,^{1, 2} Zhen-Zhen Kong,³ Gang Cao,^{1, 2, 4} Gui-Lei Wang,^{3, 4, 5} Hai-Ou Li,^{1, 2, 4, b)} and Guo-Ping Guo^{1, 2, 4, 6}

¹⁾CAS Key Laboratory of Quantum Information, University of Science and Technology of China, Hefei, Anhui 230026, China

²⁾CAS Center for Excellence and Synergetic Innovation Center in Quantum Information and Quantum Physics, University of Science and Technology of China, Hefei, Anhui 230026, China

³⁾Key Laboratory of Microelectronics Devices & Integrated Technology, Institute of Microelectronics, Chinese Academy of Sciences, Beijing 100029, China

⁴⁾Hefei National Laboratory, University of Science and Technology of China, Hefei 230088, China

⁵⁾Beijing Superstring Academy of Memory Technology, Beijing 100176, China

⁶⁾Origin Quantum Computing Company Limited, Hefei, Anhui 230026, China

(Dated: 24 March 2023)

Spin qubits based on silicon-metal-oxide-semiconductor (Si-MOS) quantum dots (QDs) are promising platforms for large-scale quantum computers. To control spin qubits in QDs, electric dipole spin resonance (EDSR) has been most commonly used in recent years. By delocalizing an electron across a double quantum dots (DQD) charge state, "flopping-mode" EDSR has been realized in Si/SiGe QDs. Here, we demonstrate a flopping-mode spin qubit in a Si-MOS QD via Elzerman single-shot readout. When changing the detuning with a fixed drive power, we achieve s-shape spin resonance frequencies, an order of magnitude improvement in the spin Rabi frequencies, and virtually constant spin dephasing times. Our results offer a route to large-scale spin qubit systems with higher control fidelity in Si-MOS QDs.

Spin qubits in silicon QDs are a leading candidate for building a quantum processor due to their long coherence time^{1,2}, potential scalability^{3,4}, and compatibility with advanced semiconductor manufacturing technology⁵⁻⁷. Currently, as an alternative to implementing electron spin resonance (ESR)⁸⁻¹³, EDSR allows the single-qubit and two-qubit operation fidelities to achieve 99.9%^{14,15} and 99%¹⁶⁻¹⁸, respectively, and allows for qubit operation at higher temperatures¹⁹.

To implement EDSR in Si-MOS QDs, a rectangular micromagnet is deployed to generate an inhomogeneous magnetic field and an oscillating electric field resonant with the Larmor frequency is coupled to drive the spin states²⁰⁻²³. During the conventional EDSR measurement, electrons in Si-MOS QD are confined in the quantum well, leading to a relatively small electric dipole^{24,25}. Driving single spin rotations in a DQD close to zero detuning where electron shuttles between two QDs, the "flopping-mode" EDSR increases the electric dipole in QDs²⁶. A longer spin coherence time (T_2^{Rabi}) with the same Rabi oscillation frequency (f_{Rabi}) has been achieved in Si/SiGe spin qubits by applying flopping-mode EDSR via dispersive readout²⁷. However, the small size and complicated distribution of Si-MOS QDs make cavity readout of a flopping-mode spin qubit in Si-MOS QDs difficult^{1,9-11,13,19,21}.

Here, we demonstrate a flopping-mode single spin qubit in a Si-MOS QD via the Elzerman single-shot readout²⁸. By setting gate voltages carefully, a DQD with appropriate tunneling rates of an electron from the QD to the reservoir is formed underneath adjacent electrodes. Then, we measure the EDSR spectra, Rabi oscillation, and Ramsey fringes. Due to

the large interdot tunnel coupling $2t_c$, an s-shape spin resonance frequency (f_q) as a function of the energy detuning (ϵ) is formed. We achieve an order of magnitude improvement in f_{Rabi} around $\epsilon = 0$ with the spin dephasing times (T_2^*) and spin coherence time of Rabi oscillation (T_2^{Rabi}) virtually constant.

Fig. 1(a) shows a scanning electron microscope (SEM) image of a typical Si-MOS DQD device, nominally identical to the one measured in Ref.²³. The device was fabricated on a natural silicon substrate with a 70 nm thick isotopically enriched ²⁸Si epi layer that has a residual ²⁹Si concentration of 60 ppm. Overlapping aluminum gate electrodes were fabricated using multi-layer gate stack technology²⁹. The cobalt micromagnet integrated near QDs will be fully magnetized during the measurement, leading to a transverse magnetic field gradient for driving the spin qubits²². The total magnetic field at the QDs (B_{total}) is the sum of the external magnetic field B_{ext} and the stray field from the micromagnet, as shown in the right bottom corner of Fig. 1(a). The device is in a dilution refrigerator at an electron temperature of $T_e = 182.7 \pm 0.6$ mK (see Sec. S2 in the Supplementary Materials for details).

The electrons are confined in the potential wells under gates LP and BC and form the DQD by selectively tuning gates LP, LB, and BC, as shown in Fig. 1(d). The corresponding charge stability diagram is shown in Fig. 1(b). (N_1, N_2) on the diagram labels the corresponding number of electrons. The black arrow illustrates the direction of ϵ between the DQD. Gates MC and BC are designed to create a channel under the lead gate LG for electrons to tunnel between the electron reservoir and the DQD. Due to the small electrode size (~ 30 nm) and the difference in the thermal expansion coefficient between the aluminum electrodes and SiO₂ substrate surface, there is usually one quantum-well formed under each electrode gate in Si-MOS QDs, possibly forming complicated quadruple or more quantum dots in the device designed for the DQD.

^{a)}These authors contributed equally to this work.

^{b)}Corresponding author: haiouli@ustc.edu.cn

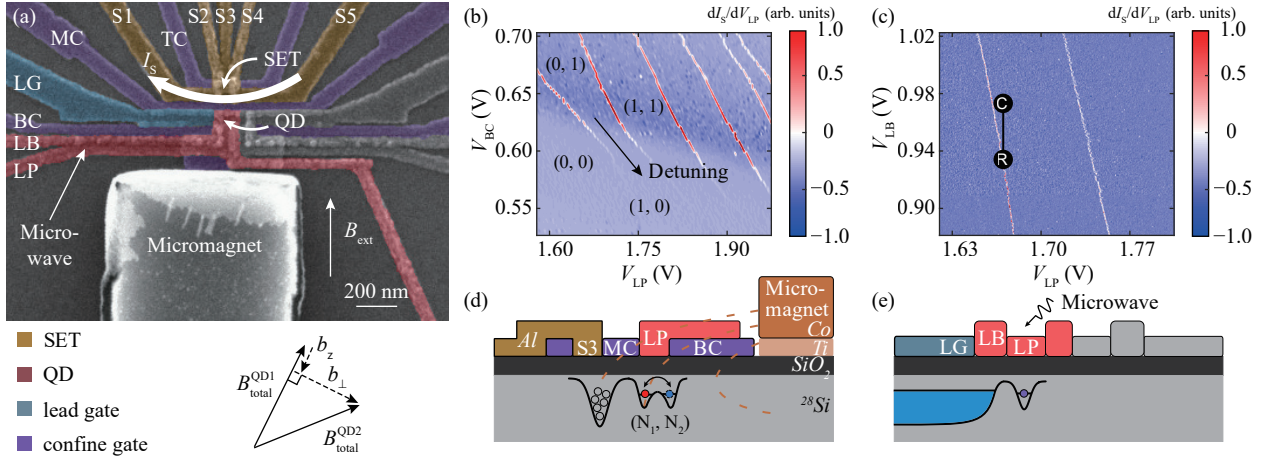


FIG. 1. Flopping-mode spin qubit device layout and operation. (a) False-color SEM image of the device. The DQD is formed underneath gates LP (red) and BC (blue). The confine gates TC, MC and BC (purple) laterally confine the QDs and the single-electron transistor (SET). The positions of QDs and SET are indicated by two white thin arrows. The lead gate LG (blue) is the reservoir gate supplying electrons for the QDs. The SET is tuned by setting the voltages of the yellow gates S1 to S5 as a charge sensor of QDs. The white bold arrow above the SET indicates the SET current (I_S) direction. Gate LP (red) is connected to impedance-matched high-frequency lines via cryogenic bias-tees. The left white arrow indicates that microwaves are applied to gate LP. The right white arrow indicates the direction of the external magnetic field (B_{ext}). The cobalt (Co) rectangular micromagnet at the bottom of the image is used to generate an inhomogeneous magnetic field. The total magnetic field (B_{total}) contains B_{ext} and the magnetization field of the micromagnet. The difference in B_{total} between two QDs can be divided into longitude (b_z) and transverse (b_{\perp}) components. (b) Charge stability diagram of the DQD measured by differentiating I_S as a function of gate voltages V_{LP} and V_{BC} . The electron numbers in the QD underneath gates LP and BC are labeled (N_1, N_2) on the diagram. The direction of the energy detuning (ϵ) in the DQD is indicated by the black dashed arrow. (c) Charge stability diagram of the DQD as a function of gate voltages V_{LP} and V_{LB} . We apply two-step pulse sequences to gate LB for the Elzerman single-shot readout. The relative voltage magnitude at each step of the pulse sequence for qubit manipulation is illustrated by the black line between two circles. During the measurement, we calibrate V_{LB} , V_{LP} and V_{BC} to maintain the tunneling rate of the electron from the DQD to the reservoir at the transition line. (d) Cross-sectional schematics of the device fabricated on a purified silicon-28 epi-layer. Electrons confined in the left quantum well underneath the SET gates S3 (yellow) are sensitive to charge movement in the QD region. The red (N_1) and blue (N_2) circles on the right side of the quantum wells represent the electrons in the flopping-mode regime. (e) Cross-sectional schematics of the device along the perpendicular direction. The electrons in the DQD tunnel across the barrier under gate LP to the reservoir under lead gate LG. The microwave is applied to gate LP to rotate the electron spin, as mentioned in (a).

Then, we apply two-step pulse sequences to gate LB for the Elzerman single-shot readout, as shown by points R (Read) and C (Control) in Fig. 1(c). The gate LB is designed to modify the tunneling rate of electrons from the DQD to the electron reservoir, as shown in Fig. 1(e). Due to the capacitive coupling between gate LB, LP and BC, we need to calibrate the gate voltages V_{LB} , V_{LP} and V_{BC} to maintain the tunneling rate for different ϵ during the measurements. We confirm that the transitions between points R and C are adiabatic, as discussed in Sec. S3 in the Supplementary Materials.

An external magnetic field is applied to the device for Elzerman single-shot readout. B_{ext} is set to 605 mT to induce Zeeman splitting between spin states and fully magnetize the micromagnet magnetic field. As a result, ~ 20 GHz microwave pulses are applied to the LP gate via a cryogenic bias-tee to manipulate the qubit. By using sequences of selective EDSR pulses with microwave burst of frequency (f_s) at point C, we can perform single-qubit operations on the electron. The spin state is read out via state-to-charge conversion at point R, and a $|\downarrow\rangle$ electron is selectively loaded for initialization in the next pulse sequence²³. The details of the measurement circuits are discussed in Sec. S1 in the Supplementary Materials.

To detect the EDSR spectra rapidly, we apply frequency-chirped microwave pulses (± 2 MHz around the center frequencies (f_s), 100 μ s duration times) to gate LP before the end of the control phase^{23,30–32}. If the frequency sweeps through the spin resonance frequencies f_q , the electron spin will end up in the excited state $|\uparrow\rangle$. By selectively setting V_{LP} , V_{LB} , and V_{BC} , we perform the Elzerman readout with a fixed tunneling rate of approximately 150 Hz for the $|\downarrow\rangle$ electron to ensure consistency in the readout process while ϵ increases from -4.5 to 4.5 meV along the exact transition line (0, 1) to (1, 0) (see Sec. S2 in the Supplementary Materials for details). We measure the probability of electrons in the excited state (P_{\uparrow}) as a function of f_s from 300 repeated single-shot readouts. For each ϵ , we repeat the measurement ten times, as mentioned in Ref.²⁹. The EDSR spectra over ϵ from -4.5 to 4.5 meV are shown in Fig. 2(b). There is an s-shape curve of increased P_{\uparrow} with a width of 4 MHz of f_s , where f_q is located. We calibrate the peak of P_{\uparrow} and extract f_q as a function of ϵ in Fig. 2(c).

To explain this s-shape feature, we focus on the Hamiltonian H of a single-electron occupied DQD system on the basis

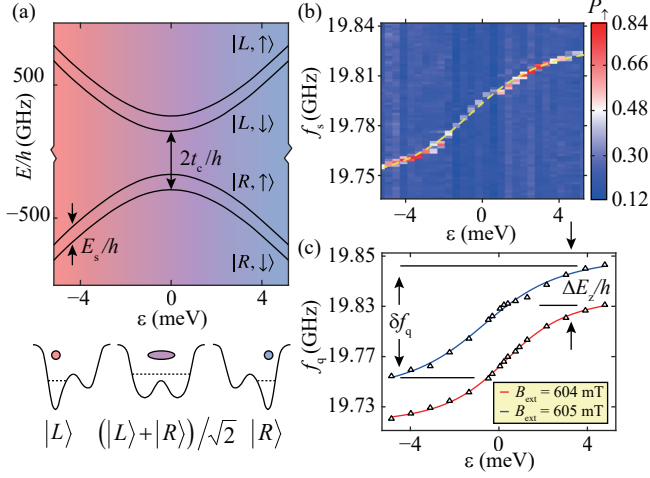


FIG. 2. (a) Top: The eigenenergies calculated by diagonalizing the Hamiltonian in Eq. 1. Bottom: Schematics of the potential well for far detuned (left and right) and flopping-mode (middle) regimes. (b) EDSR spectra for the probability of $|\uparrow\rangle$ electrons (P_\uparrow) as a function of both ε and microwave frequency (f_s). The dashed curve marks the position of increased P_\uparrow , which represents coarse ranges of spin resonance frequency (f_q). (c) f_q as a function of ε for $B_{\text{ext}} = 604$ mT (red) and $B_{\text{ext}} = 605$ mT (blue). The left arrows indicate the Zeeman energy difference (δf_q) generated by the longitudinal magnetic field difference (b_z) of the micromagnet. The right arrows illustrate the splitting energy difference (ΔE_z) for different B_{ext} .

$(|L \downarrow\rangle, |L \uparrow\rangle, |R \downarrow\rangle, |R \uparrow\rangle)$ ^{26,33}:

$$H = \frac{1}{2} \begin{pmatrix} -\varepsilon - E_{z1} & -2t_{\text{SO}} & 2t_c & 0 \\ -2t_{\text{SO}} & -\varepsilon + E_{z1} & 0 & 2t_c \\ 2t_c & 0 & \varepsilon - E_{z2} & 2t_{\text{SO}} \\ 0 & 2t_c & 2t_{\text{SO}} & \varepsilon + E_{z2} \end{pmatrix}. \quad (1)$$

Here, E_{z1} and E_{z2} are Zeeman energies for the first and second QD, respectively, $2t_c$ is the interdot tunnel coupling, and $2t_{\text{SO}} = g\mu_B b_\perp$ is the synthetic spin-orbit coupling induced by the transverse magnetic field difference (b_\perp).

The eigenenergies of this four-level system are shown in Fig. 2(a). The avoided crossings at $\varepsilon = 0$ are generated by $2t_c$. By diagonalizing the Hamiltonian in Eq. (1), we calculate the energy splitting (E_s) between the lowest two energy levels as a function of ε . Therefore, the corresponding spin resonance frequency of the qubit is obtained through $f_q \equiv E_s/h$. For the situation of a small inhomogeneous field, i.e., $b_{\perp,z} \ll |\Omega - E_z|/g\mu_B$, where $\Omega = \sqrt{\varepsilon^2 + 4t_c^2}$, E_s is corrected by the transverse and longitude gradients to second and first order, respectively²⁶:

$$E_s \simeq E_z - \frac{E_z^2 - \varepsilon^2}{2E_z(\Omega^2 - E_z^2)}(g\mu_B b_\perp)^2 - \frac{\varepsilon}{\Omega}g\mu_B b_z. \quad (2)$$

Here, $E_z = (E_{z1} + E_{z2})/2$ is the averaged Zeeman energy, and $\delta E_z = (E_{z1} - E_{z2})/2 = g\mu_B b_z$ is the Zeeman energy difference generated by the longitudinal magnetic field difference (b_z) of the micromagnet.

We plot f_q as a function of ε for $B_{\text{ext}} = 605$ and 604 mT in Fig. 2(c). By fitting f_q with Eq 2, we obtain $2t_c/h =$

914 ± 167 and 705 ± 40 GHz for $B_{\text{ext}} = 605$ and 604 mT, respectively. The difference between the fitted splitting energy ($\Delta E_z = 19.790 \pm 0.002 - 19.760 \pm 0.001$ GHz) equals the difference between the external magnetic fields ($g\mu_B \Delta B_{\text{ext}}/h = 28$ MHz). $\delta f_q \equiv 2\delta E_z/h = 56.8 \pm 4.5$ MHz for far detuned limits is shown in Fig. 2(c). In Ref.²⁷, the lowest E_s occurs near $\varepsilon = 0$, leading to a sweet spot for spin dephasing. However, in our device $2t_c \gg E_z$, the second-order item $\frac{E_z^2 - \varepsilon^2}{2E_z(\Omega^2 - E_z^2)}(g\mu_B b_\perp)^2$ in Eq 2 is suppressed, and there is no sweet spot approximately $\varepsilon = 0$.

After calibrating f_q , we now use a microwave burst with a specific burst time (τ_B) to manipulate the spin qubit. First, we measure P_\uparrow as a f_s function with a fixed τ_B . Each point of P_\uparrow in the curve is averaged from 300 repeated single-shot readouts. Then, we repeat the measurement ten times and sum P_\uparrow with τ_B changing from 0 to 4 μs . The Rabi chevron is plotted in Fig. 3(a).

Fig. 3(b) illustrates f_{Rabi} as a function of ε with fixed microwave power $P_{\text{MW}} = 0$ dBm at the source. f_{Rabi} is symmetric about $\varepsilon = 0$ and is an order of magnitude larger at $\varepsilon = 0$ than the far detuned position. For every ε , the corresponding f_{Rabi} is extracted by fitting the Rabi oscillation with the function $P_\uparrow(\tau_B) = A \cdot \exp(-\tau_B/T_2^{\text{Rabi}}) \cdot \sin(f_{\text{Rabi}}\tau_B)$, as shown in Fig. 3(c).

For a typical flopping-mode EDSR process, Ref²⁶ gives f_{Rabi} as a function of ε for small b_\perp :

$$f_{\text{Rabi}} = 4t_c^2 g\mu_B b_\perp \Omega_c / \Omega |\Omega^2 - E_z^2|. \quad (3)$$

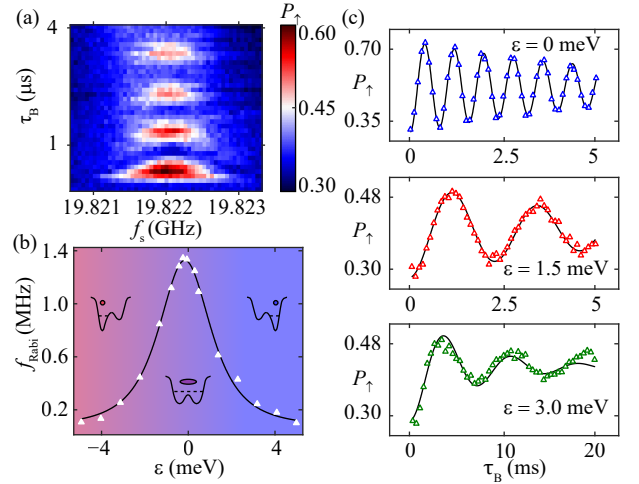


FIG. 3. (a) The Rabi chevron is acquired at $\varepsilon = 0.5$ meV. Every point of P_\uparrow is obtained by repeating the pulse sequence 300 times with τ_B fixed. We sweep the microwave frequencies, repeat the measurement 10 times for every τ_B , and finally sum the results. (b) The Rabi frequency (f_{Rabi}) is plotted as a function of ε with fixed microwave power. f_{Rabi} is an order of magnitude larger at approximately $\varepsilon = 0$ than at the far detuned position. The solid curve is the fitting result of Eq. 3. (c) Rabi oscillations obtained at different ε . Top panel: $\varepsilon = 0$ meV, $f_{\text{Rabi}} = 1.262 \pm 0.002$ MHz and $T_2^{\text{Rabi}} = 6.46 \pm 0.39$ μs ; Middle panel: $\varepsilon = 1.5$ meV, $f_{\text{Rabi}} = 0.429 \pm 0.003$ MHz and $T_2^{\text{Rabi}} = 5.53 \pm 0.57$ μs ; Bottom panel: $\varepsilon = 3.0$ meV, $f_{\text{Rabi}} = 0.135 \pm 0.003$ MHz and $T_2^{\text{Rabi}} = 7.01 \pm 0.82$ μs .

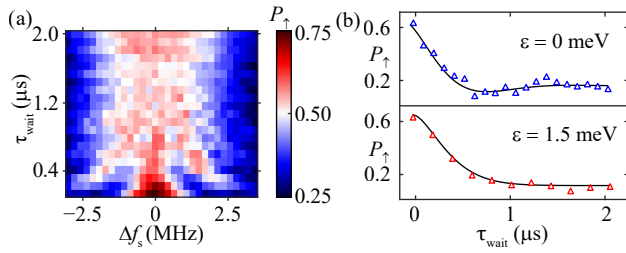


FIG. 4. (a) Ramsey fringes as a function of frequency detuning (Δf_s) and waiting time (τ_{wait}) measured at $\varepsilon = 0.5$ meV by applying a standard Ramsey fringe sequence with two $\pi/2$ pulses. Every point of P_\uparrow is obtained by repeating the pulse sequence 300 times. We repeat the measurement ten times for every τ_{wait} and sum the results. (b) The spin dephasing times (T_2^*) were measured through Ramsey fringes for different ε . Top panel: $\varepsilon = 0$ meV, $T_2^* = 0.42 \pm 0.31$ μs ; Bottom panel: $\varepsilon = 1.5$ meV, $T_2^* = 0.43 \pm 0.02$ μs .

Here, $\Omega_c = edE_{ac}/\hbar$ is the Rabi frequency of charge qubits, proportional to the distance between the two QDs d , and the electric field with amplitude E_{ac} . $\Omega_c = 15.8 \pm 0.8$ GHz can be obtained from the relevant result of f_{Rabi} with a $g\mu_B b_\perp$ estimated as 0.232 μeV ²². We estimate $d \sim 0.02$ μm , thus $b_\perp \sim 0.1$ T/ μm · 0.02 $\mu\text{m} = 2$ mT.

Fig. 3(c) shows details of the Rabi oscillations for different ε . $f_{\text{Rabi}} = 1.262 \pm 0.002$ MHz is achieved in the top panel. When ε increases to 1.5 and 3 meV, the Rabi frequencies decrease to $f_{\text{Rabi}} = 0.429 \pm 0.003$ and $f_{\text{Rabi}} = 0.135 \pm 0.003$ MHz, respectively. By fitting the Rabi oscillation to an exponentially decaying sinusoid, $T_2^{\text{Rabi}} = 6.46 \pm 0.39$ μs at $\varepsilon = 0$, $T_2^{\text{Rabi}} = 5.53 \pm 0.57$ μs at $\varepsilon = 1.5$ meV and $T_2^{\text{Rabi}} = 7.01 \pm 0.82$ μs at $\varepsilon = 3$ meV are obtained. T_2^{Rabi} is stable when ε increases.

Furthermore, we measure T_2^* for different ε through Ramsey fringes. In Fig. 4(a), the Ramsey fringes are measured in the same way as the Rabi chevron. The averaged $T_2^* = 0.42$ μs for $\varepsilon = 0$ and 1.5 meV is acquired as shown in Fig. 4(b). As mentioned in Ref.²², the longitudinal magnetic field difference b_z is one of the most relevant sources for dephasing in our device. Since the sweet spot is absent and b_z is constant during the measurement, we attribute the enhancement of the quality factor ($Q \equiv 2T_2^{\text{Rabi}} f_{\text{Rabi}}$) to the improvement of the electric dipole.

In summary, we demonstrate the flopping-mode EDSR in a Si-MOS quantum dot through the Elzerman single-shot readout. We construct a DQD with $2t_c/h \sim 800$ GHz under adjacent electrodes by selectively setting gate voltages. We extract an s-shape f_q as a function of ε from the EDSR spectra. Then, we improve f_{Rabi} by an order of magnitude from 0.135 ± 0.003 to 1.262 ± 0.002 MHz by increasing the electric dipole. T_2^* and T_2^{Rabi} remains at approximately 0.42 ± 0.03 μs and 6.46 ± 0.39 μs , respectively. We anticipate that flopping-mode EDSR will have better performance in the heavy hole regime³⁴ or phosphorus donor qubits³⁵, and will perform two-qubit operation³⁶ in the future.

SUPPLEMENTARY MATERIALS

See the supplementary material for the description on the device, measurement setup, background subtraction and simulation in more detail. The larger charge stability diagram and the method for extracting the coupling strength are also presented.

ACKNOWLEDGMENTS

This work was supported by the National Natural Science Foundation of China (Grants No. 12074368, 92165207, 12034018 and 61922074), the Innovation Program for Quantum Science and Technology (Grant No. 2021ZD0302300), the Anhui Province Natural Science Foundation (Grants No. 2108085J03), and the USTC Tang Scholarship. This work was partially carried out at the USTC Center for Micro and Nanoscale Research and Fabrication.

REFERENCES

- ¹M. Veldhorst, J. C. C. Hwang, C. H. Yang, *et al.*, “An addressable quantum dot qubit with fault-tolerant control-fidelity,” *Nature Nanotechnology* **9**, 981–985 (2014).
- ²M. Veldhorst, C. H. Yang, J. C. C. Hwang, *et al.*, “A two-qubit logic gate in silicon,” *Nature* **526**, 410–414 (2015).
- ³L. M. K. Vandersypen, H. Bluhm, J. S. Clarke, *et al.*, “Interfacing spin qubits in quantum dots and donors—hot, dense, and coherent,” *npj Quantum Information* **3**, 34 (2017).
- ⁴R. Li, L. Petit, D. P. Franke, *et al.*, “A crossbar network for silicon quantum dot qubits,” *Science Advances* **4**, eaar3960 (2018).
- ⁵L. C. Camenzind, S. Geyer, A. Fuhrer, *et al.*, “A hole spin qubit in a fin field-effect transistor above 4 kelvin,” *Nature Electronics* **5**, 178 (2022).
- ⁶A. M. J. Zwerver, T. Krahenmann, T. F. Watson, *et al.*, “Qubits made by advanced semiconductor manufacturing,” *Nature Electronics* **5**, 184–190 (2022).
- ⁷X. Zhang, H.-O. Li, G. Cao, *et al.*, “Semiconductor quantum computation,” *National Science Review* **6**, 32 (2019).
- ⁸F. H. Koppens, C. Buizert, K. J. Tielrooij, *et al.*, “Driven coherent oscillations of a single electron spin in a quantum dot,” *Nature* **442**, 766 (2006).
- ⁹W. Huang, C. H. Yang, T. Tantau, *et al.*, “Fidelity benchmarks for two-qubit gates in silicon,” *Nature* **569**, 532 (2019).
- ¹⁰L. Petit, H. G. J. Eenink, M. Russ, *et al.*, “Universal quantum logic in hot silicon qubits,” *Nature* **580**, 355–359 (2020).
- ¹¹K. W. Chan, H. Sahasrabudhe, W. Huang, *et al.*, “Exchange coupling in a linear chain of three quantum-dot spin qubits in silicon,” *Nano Letters* **21**, 1517 (2021).
- ¹²M. T. Madzik, S. Asaad, A. Youssry, *et al.*, “Precision tomography of a three-qubit donor quantum processor in silicon,” *Nature* **601**, 348–353 (2022).
- ¹³W. Gilbert, T. Tantau, W. H. Lim, *et al.*, “On-demand electrical control of spin qubits,” *arXiv preprint*, 2201.06679 (2022).
- ¹⁴K. W. Chan, W. Huang, C. H. Yang, *et al.*, “Assessment of a silicon quantum dot spin qubit environment via noise spectroscopy,” *Phys. Rev. Applied* **10**, 044017 (2018).
- ¹⁵J. Yoneda, K. Takeda, T. Otsuka, *et al.*, “A quantum-dot spin qubit with coherence limited by charge noise and fidelity higher than 99.9%,” *Nature Nanotechnology* **13**, 102–106 (2018).
- ¹⁶X. Xue, M. Russ, N. Samkharadze, *et al.*, “Quantum logic with spin qubits crossing the surface code threshold,” *Nature* **601**, 343–347 (2022).
- ¹⁷A. Noiri, K. Takeda, T. Nakajima, *et al.*, “Fast universal quantum gate above the fault-tolerance threshold in silicon,” *Nature* **601**, 338–342 (2022).

- ¹⁸A. R. Mills, C. R. Guinn, M. J. Gullans, *et al.*, “Two-qubit silicon quantum processor with operation fidelity exceeding 99%,” *Science Advances* **8**, eabn5130 (2022).
- ¹⁹C. H. Yang, R. C. C. Leon, J. C. C. Hwang, *et al.*, “Operation of a silicon quantum processor unit cell above one kelvin,” *Nature* **580**, 350–354 (2020).
- ²⁰E. I. Rashba and A. L. Efros, “Orbital mechanisms of electron-spin manipulation by an electric field,” *Phys. Rev. Lett.* **91**, 126405 (2003).
- ²¹R. C. C. Leon, C. H. Yang, J. C. C. Hwang, *et al.*, “Coherent spin control of s-, p-, d- and f-electrons in a silicon quantum dot,” *Nature Communications* **11**, 797 (2020).
- ²²X. Zhang, Y. Zhou, R.-Z. Hu, *et al.*, “Controlling synthetic spin-orbit coupling in a silicon quantum dot with magnetic field,” *Phys. Rev. Applied* **15**, 044042 (2021).
- ²³R.-Z. Hu, R.-L. Ma, M. Ni, *et al.*, “An operation guide of si-mos quantum dots for spin qubits,” *Nanomaterials* **11**, 2486 (2021).
- ²⁴M. Pioro-Ladrière, T. Obata, Y. Tokura, *et al.*, “Electrically driven single-electron spin resonance in a slanting Zeeman field,” *Nature Physics* **4**, 776–779 (2008).
- ²⁵E. Kawakami, P. Scarlino, D. R. Ward, *et al.*, “Electrical control of a long-lived spin qubit in a Si/SiGe quantum dot,” *Nature Nanotechnology* **9**, 666–670 (2014).
- ²⁶M. Benito, X. Croot, C. Adelsberger, *et al.*, “Electric-field control and noise protection of the flopping-mode spin qubit,” *Phys. Rev. B* **100**, 125430 (2019).
- ²⁷X. Croot, X. Mi, S. Putz, *et al.*, “Flopping-mode electric dipole spin resonance,” *Phys. Rev. Research* **2**, 012006 (2020).
- ²⁸J. M. Elzerman, R. Hanson, L. H. Willems van Beveren, *et al.*, “Single-shot read-out of an individual electron spin in a quantum dot,” *Nature* **430**, 431 (2004).
- ²⁹X. Zhang, R.-Z. Hu, H.-O. Li, *et al.*, “Giant Anisotropy of Spin Relaxation and Spin-Valley Mixing in a Silicon Quantum Dot,” *Phys. Rev. Lett.* **124**, 257701 (2020).
- ³⁰M. Shafiei, K. C. Nowack, C. Reichl, *et al.*, “Resolving Spin-Orbit- and Hyperfine-Mediated Electric Dipole Spin Resonance in a Quantum Dot,” *Phys. Rev. Lett.* **110**, 107601 (2013).
- ³¹A. Laucht, R. Kalra, J. T. Muhonen, *et al.*, “High-fidelity adiabatic inversion of a ³¹P electron spin qubit in natural silicon,” *Applied Physics Letters* **104**, 092115 (2014).
- ³²A. Sigillito, J. Loy, D. Zajac, *et al.*, “Site-Selective Quantum Control in an Isotopically Enriched ²⁸Si/Si_{0.7}Ge_{0.3} Quadruple Quantum Dot,” *Phys. Rev. Applied* **11**, 061006 (2019).
- ³³M. Benito, X. Mi, J. M. Taylor, *et al.*, “Input-output theory for spin-photon coupling in Si double quantum dots,” *Phys. Rev. B* **96**, 235434 (2017).
- ³⁴P. M. Mutter and G. Burkard, “Natural heavy-hole flopping mode qubit in germanium,” *Phys. Rev. Research* **3**, 013194 (2021).
- ³⁵F. Krauth, S. Gorman, Y. He, *et al.*, “Flopping-mode electric dipole spin resonance in phosphorus donor qubits in silicon,” *Phys. Rev. Applied* **17**, 054006 (2022).
- ³⁶J. Cayao, M. Benito, and G. Burkard, “Programmable two-qubit gates in capacitively coupled flopping-mode spin qubits,” *Phys. Rev. B* **101**, 195438 (2020).